Two Dimensional Transport Study of Scrape off Layer Plasmas

YAMAMOTO, Nobuyuki
Interdisciplinary Graduate School of Advanced Energy Engineering Sciences, Kyushu University

YAGI, Masatoshi
Research Institute for Applied Mechanics, Kyushu University

ITOH, Sanae-I.
Research Institute for Applied Mechanics, Kyushu University

https://doi.org/10.15017/6766040

出版情報：九州大学応用力学研究所所報. 117, pp.37-52, 1999-09. Research Institute for Applied Mechanics, Kyushu University
バージョン：
権利関係：

Two Dimensional Transport Study of Scrape off Layer Plasmas

Nobuyuki YAMAMOTO*1, Masatoshi YAGI*2
and Sanae-I. ITOH*2
E-mail of corresponding author: *yagi@riam.kyushu-u.ac.jp*

(Received April 12, 1999)

Abstract

Two dimensional transport code is developed to analyze the heat pulse propagation in the scrape-off layer plasma. The classical and anomalous transport models are considered as a thermal diffusivity perpendicular to the magnetic field. On the other hand, the classical transport model is chosen as a thermal diffusivity parallel to the magnetic field. The heat deposition profiles are evaluated for various kinds of transport models. It is found that the heat pulse which arraives at the divertor plate due to the classical transport is largest compared with other models. The steady state temperature profiles of the electron and ion are also discussed.

Key words : *The scrape-off layer, H-mode, ELMs, Detached divertor, Anormalous transport*

1. Introduction

There are many technical issues to overcome serious engineering problems to realize controlled nuclear fusion. One of the most difficulties of such challenges is related to the close proximity of material surfaces, virtually at room temperature, with a hot thermonuclear plasma. At the beginning of magnetic fusion research, divertors have been proposed to isolate the surface contacted with the plasma and vessel wall and to allow the removal of the helium ash. In this idea, the main plasma is surrounded by the scrape-off layer (SOL) which doesn't map out closed surfaces like those within the plasma, and the open field lines of the scrape-off layer are guided into a divertor chamber separated from the main plasma chamber and intercepted there by target plate.

The crucial tasks to develop the divertor can be divided into four main areas:

(1) the wide disposal of plasma power exhausted from the main plasma,

(2) the production of sufficiently high gas pressures in the vicinity of pump ducts to enable the removal of fuel and helium (ash) gas from the system,

(3) the elimination or reduction of impurity production,

(4) the screening of impurities produced at the plasma boundary, or intentionally added, from the plasma core.

For this object, the experiment of the detached divertor is practiced.

And with these conditions, good core confinement and relatively high core plasma density should be maintained to enhance fusion reactivity. The H-mode plasma is considered to satisfy this condition.

In addition to simultaneously satisfying the above criteria, it is necessary to understand the detailed physics of divertor operation. For this purpose, we solve the transport equation for the various transport models in the SOL region.

The organization of this paper is as follows. In Chapter 2, we survey the experimental results about the detached divertor and the H-mode plasma, and also the transport models in the SOL region. In chapter 3, we give the analytic solution in the SOL region for the various transport models, and also we solve the time dependent transport equation for the electron and the ion, and examine the heat pulse propagation in the SOL region. Summary and discussions will be given in Chapter 4.

*1 Interdisciplinary Graduate School of Advanced Energy Engineering Sciences, Kyushu University
*2 Research Institute for Applied Mechanics, Kyushu University

2. Review

2.1 Divertor Experiments

2.1.1 Edge localized mode

The H-mode of neutral-beam-heated divertor discharges was discovered in ASDEX [1, 2] and later also found in Doublet-III [3] and PDX [4]. This mode has attracted great attention, since it recovers the energy and particle confinement times of Ohmically heated plasmas. A well-known signature of these H-discharges are the so-called H_α-bursts, which indicate repetitive particle and energy losses from the plasma periphery due to the Edge localized modes (ELMs). H-mode plasma with completely ELM free has a good particle confinement time so that impurities accumulate in the plasma, which ultimately attains levels of radiated power from inside the plasma and leads to quench the H-mode [5] . Since ELM event can expel significant numbers of impurities, there is a possibility that radiation collapse and MHD collapse are avoidable. The stationary operation of ELMy H-modes is considered for ITER burn scenario.

However, a large amount of particle and heat flux bursts out from the main plasma, which burdens serious heat loads on divertor plate.

In this section, based on the experimental results, we discuss the effects of ELMs on the SOL plasmas.

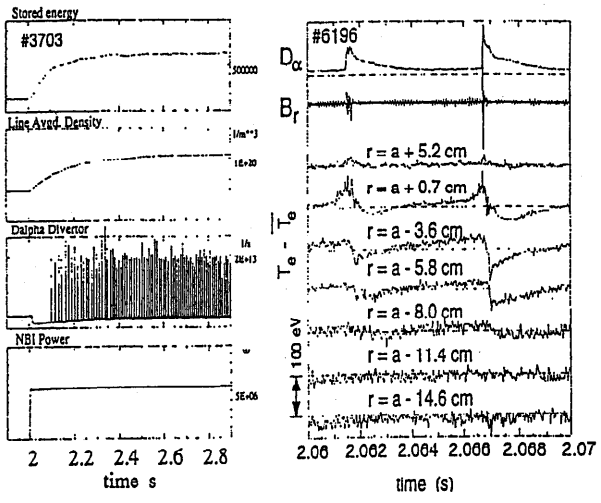

Fig. 1 Time trace from Elmy H-mode discharges in ASDEX Upgrade.(cited from Ref.[6]

Figure 1 shows time traces from ELMy H-mode discharges in ASDEX Upgrade [6]. In the right part of figure 1, the temporal evolution of the D_α line and the electron temperature at the plasma edge are shown. The location of the separatrix is at $r = a$. From the D_α line, we see that the ELM event is start, so the particle and energy in the bulk plasma are expelled to the SOL region. Outside the separatrix, T_e increases during the ELM, indicating that the rapid outward transport induced by ELM leads to a temporary heating of the SOL plasma. And inside the separatrix, the effect of the ELMs is to rapidly reduce T_e. It can be seen that the effect of ELMs is really 'edge localized', i.e. T_e is not affected inside a certain radius r_{ELM} (in the case shown in the figure 1, $\frac{r_{ELM}}{a} \approx 0.8$). In addition, Figure 1 shows the fluctuation magnetic field at the outside midplane of torus. During ELMs, there is a high level of magnetic fluctuations, indicating that the rapid enhancement of transport is due to an MHD instability.

From the the D_α line at the divertor plate shown in the left part of figure 1, we see that this energy bursted from the main plasma is transported through the SOL region to the divertor region. Figure 2 shows power

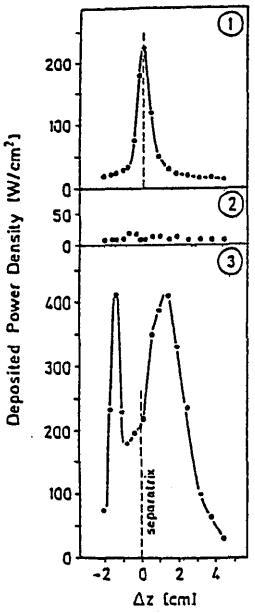

Fig. 2 Power deposition profiles along the poloidal direction of the divertor plate:(1)L-phase;(2)quiet H phase between bursts;(3)at burst maximum.(cited from Ref.[7]).

deposition profiles along the poloidal direction of the divertor plate for the L phase, the quiescent H phase between bursts and the burst maximum [7]. The power deposition profile in the L phase is localized at the separatrix. During the quiescent H phase, the power deposition on the divertor plates nearly vanishes. During the bursts, the power is deposited in the more wide range than that in the L phase. And also the peak of the deposited power density is about two times larger than that in the L phase. Such a large heat load promotes impurity production. To avoid this situation, various experiments have been done to find the solution. Next section, for this example, we explain the detached divertor experiment.

2.1.2 Detached Divertor

In the recent years it has become evident that the problems of power deposition and wall erosion are of paramount interest to be addressed for the development of next-step tokamak devices such as ITER. While the high recycling divertor regime may be a marginally acceptable regime of operation from the viewpoint of power handling, the erosion associated with the large incident ion fluxes may limit seriously the lifetime of the divertor target, making the applicability of the high recycling divertor questionable for next step devices.

Furthermore, if the high recycling regime is extrapolated to some of the operating modes proposed for ITER, the power deposited onto the divertor by the recombining ions and electrons in the material surface will exceed the steady-state power handling capability of the divertor target.

As a solution to these two problems, the so-called "detached" divertor regime was first proposed to be the preferred divertor regime of a next-step device.

The basic physical features of the detached divertor rely upon the transfer of parallel momentum from the plasma to the recycling neutral atoms and subsequently to the divertor target and vessel walls. This has two important effects: the plasma pressure at the divertor is reduced with respect to that expected from the high recycling regime and together with ionization losses and impurity radiation, it leads to low electron temperature at the divertor which allow volume recombination processes to take place. The combination of pressure reduction and hydrogen recombination leads to lower incident ion fluxes to the divertor target and potentially allows one to achieve higher radiative power fractions in the scrape-off layer (SOL) and divertor. This comes about because the recombination power deposited on the target decreases with the reduction of the plasma flux. A further beneficial effect of the detached divertor regime is the largest particle flux impinging on the surfaces is in the form of hydrogenic neutral atoms and molecules scattered from the plasma, which are not accelerated by the sheath potential and hence have lower energies than the corresponding ions. This minimizes the amount of physical sputtering suffered by the divertor target.

We review the divertor experiment in the JET [8].

The experimental result for the Ohmic discharges with increment of the main plasma density is shown in the figure 3 and the figure 4 . From these figures, we see that the ion flux, the plasma pressure and the temperature are decreasing and the neutral flux is increasing at the both divertor plates with the increasing main plasma density. So detached divertor condition is attained.

There was the hypothesis that enhanced perpendicular anomalous transport in the divertor chamber may explain plasma detachment. If this hypothesis is right, the vertical divertor plate is affected by the ion flux. However, the detailed divertor ion flux measurements obtained in the JET Mark I divertor have eliminated this hypothesis. This result is shown in the figure 5.

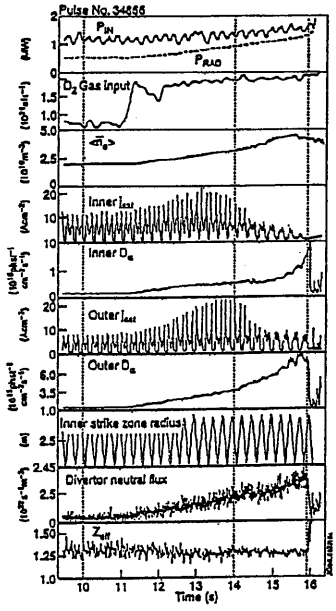

Fig. 3 Evolution of the measured core and divertor plasma parameters during an Ohmic density plasma.(cited from Ref.[8]).

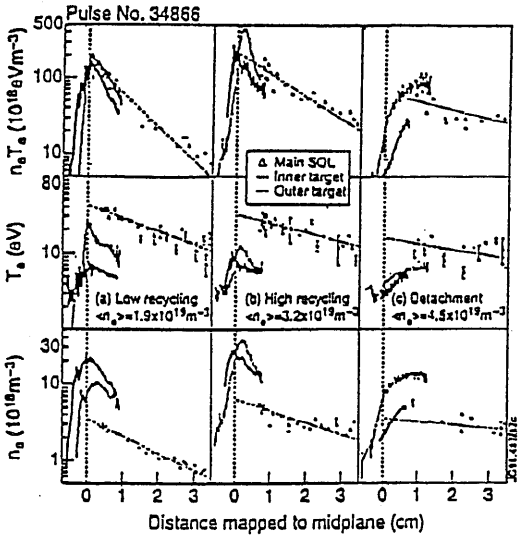

Fig. 4 Electron pressure, temperature and density in the SOL(triangle) and divertor(thick line inner divertor, thin line outer divertor) versus distance to the separatrix mapped to the outer midplane at the three different times during an Ohmic density ramp discharge: low recycling, high recycling and detached divertor.(cited from Ref.[8]).

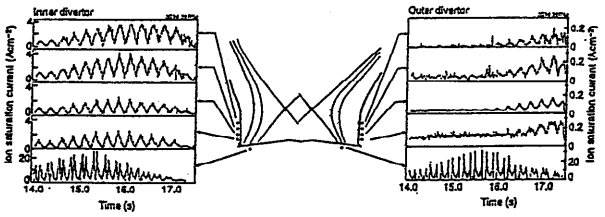

Fig. 5 Evolution of the ion flux at the inner and outer horizontal divertor plate and the inner and outer vertical plate for an Ohmic density ramp in JET.(cited from Ref.[8]).

The detached divertor condition in the H-mode plasma is also examined. Due to the presence of ELMs, the general character of H-mode discharges is different from the Ohmic case.

At the ELM events, reattachment occurs and large plasma fluxes to the target are measured. Reattachment between ELMs can be eliminated, albeit at the cost of increasing the impurity content of the main plasma. In these discharges the divertor remains detached through the H-mode phase and larger radiative losses can be achieved. Figure 6 shows the ion flux profiles measured

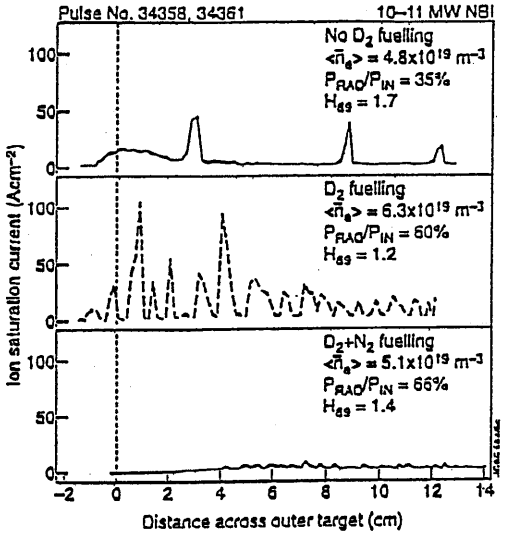

Fig. 6 Measured ion flux profiles at the divertor target for three H-mode discharges:(a) No deuterium Fuelling (b) Strong Deuterium Fuelling and (c) Deuterium and Nitrogen Fuelling.(cited from Ref.[8]).

at the divertor for three characteristic examples of (a) H-mode without gas fuelling, (b) Deuterium gas fuelled H-mode and (c) impurity seeded (Nitrogen) H-mode. The unfuelled discharge has infrequent ELMs, while the gas fuelled H-mode has a very low ion flux in-between ELMs with large fluxes at the ELMs so that divertor condition becomes detachment between ELMs and attachment at ELMs. The Nitrogen seeded discharge has very high frequency ELMs, but the divertor condition remains detached throughout.

2.2 Transport Model in the SOL region

2.2.1 Ueda code

From the very beginning of divertor research, asymmetries between the inner and outer divertors have been noticed. This has been primarily in the power deposited on divertor plates, with the outer divertor usually (but not always) receiving a large share of the power than the inner divertor. In addition, corresponding difference in divertor plasma conditions have also been observed. And the phenomena that the asymmetry is affected by the direction of the toroidal field has been reported.

Ueda has performed numerical simulation of the JFT-2M divertor experiments, and explained this effect by taking the drift heat flux into account [9, 10]. This code also takes account of the shapes of the scrape-off layer. To study neutral behavior, a Monte Calro method is utilized [11].

The set of equations for the scrape-off and divertor plasma contains a continuity equation for the ion density n_i, a momentum conservation equation governing the velocity $v_{\|}$ parallel to the magnetic field, a diffusion equation for the perpendicular velocity v_ψ, the energy conservation equation for the electron and ion temperature T_e and T_i, and quasineutrality equation for the electron density n_e:

$$\rho_e = m_e n_e, \qquad \rho_i = m_i n_i, \tag{1}$$

$$\frac{\partial \rho_i}{\partial t} + \nabla \cdot (\rho_i \mathrm{v}) = S_n, \tag{2}$$

$$\rho_i \left(\frac{\partial}{\partial t} + \mathrm{v} \cdot \nabla \right) v_{\|} = -\nabla_{\|} p - S_n v_{\|} + S_p, \tag{3}$$

$$v_\psi = -\frac{D_\psi}{n_i} \nabla_\psi n_i, \tag{4}$$

$$\begin{aligned} &\rho_i \left(\frac{\partial}{\partial t} + \mathrm{v} \cdot \nabla \right) \left(\frac{3}{2} \frac{kT_i}{m_i} + \frac{1}{2} \mathrm{v} \cdot \mathrm{v} \right) \\ &= -\nabla \cdot \left(\frac{\rho_i k T_i \mathrm{v}}{m_i} \right) - v_{\|} \cdot \nabla_{\|} \left(\frac{\rho_e k T_e}{m_e} \right) \\ &\quad -\nabla \cdot \mathrm{qi} - E_n^i S_n^i + Q_{ie} - Q_{cx}, \end{aligned} \tag{5}$$

$$\begin{aligned} &\rho_e \left(\frac{\partial}{\partial t} + \mathrm{v} \cdot \nabla \right) \left(\frac{3}{2} \frac{kT_e}{m_e} + \frac{1}{2} \mathrm{v} \cdot \mathrm{v} \right) \\ &= -\nabla \cdot \left(\frac{\rho_e k T_e \mathrm{v}}{m_e} \right) + v_{\|} \cdot \nabla_{\|} \left(\frac{\rho_e k T_e}{m_e} \right) \\ &\quad -\nabla \cdot \mathrm{qe} - E_n^e S_n^e + Q_{ei} - Q_{rad}, \end{aligned} \tag{6}$$

$$n_e = Zn_i, \tag{7}$$

where

$$\mathrm{qe} = -\chi_{\|}^{e}\nabla_{\|}(kT_e) - \chi_{\psi}^{e}\nabla_{\psi}(kT_e) - \frac{5}{2}\frac{n_e kT_e}{eB_t}(\mathrm{b}\times\nabla(kT_e)), \tag{8}$$

$$\mathrm{qi} = -\chi_{\|}^{i}\nabla_{\|}(kT_i) - \chi_{\psi}^{i}\nabla_{\psi}(kT_i) - \frac{5}{2}\frac{n_i kT_i}{eB_t}(\mathrm{b}\times\nabla(kT_i)), \tag{9}$$

$$\chi_{\|}^{e} = 3.16\frac{n_e T_e \tau_{ei}}{m_e}, \quad \chi_{\|}^{i} = 3.9\frac{n_i T_i \tau_{ii}}{m_i}, \tag{10}$$

$$\chi_{\psi}^{e} = \chi_{\psi}^{i} = 2D_B, \quad D_{\psi} = \frac{D_B}{2}, \tag{11}$$

and

$$D_B = \frac{T_e}{16B_t}. \tag{12}$$

m_e and m_i are electron mass and ion mass, respectively. p is the total pressure. ${S_n}^e$ and ${S_n}^i (= S_n)$ are the volume sources of electrons and ions, respectively. S_p is the momentum source. ${E_n}^e$ and ${E_n}^i$ are the total energies of electrons and ions, respectively. Z is the atomic number. q_e and q_i are the heat fluxes of electrons and ions, respectively. B_t is the toroidal magnetic field. b is the unit vector parallel to the magnetic field line. Q_{ei} is the electron-ion energy equilibration rate. Q_{rad} is radiation loss rate. $\chi_{\|}^{e}$ and $\chi_{\|}^{i}$ are the parallel classical heat conductivities of electrons and ions, respectively. τ_{ei} and τ_{ii} are the collision times of electrons and ions, respectively. χ_{ψ}^{e} and χ_{ψ}^{i} are the radial heat conductivities of electrons and ions, respectively. D_{ψ} is the radial anomalous diffusion coefficient. D_B is the Bohm diffusion coefficient.

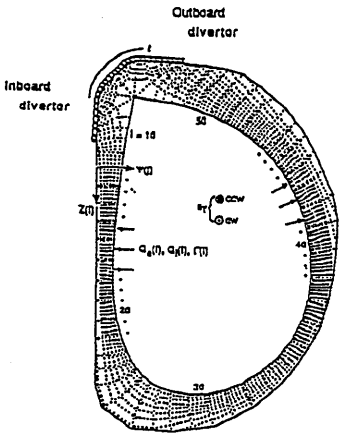

Fig. 7 Geometry, mesh and definition of the (z-ψ) co-ordinate system(cited from Ref.[9]).

The computational mesh shown in Fig 7 contains three boundaries for the fluid equations: the surface of the divertor plate, the surface of the vacuum vessel and the periphery of the core plasma. The boundary conditions are as follows.

[1] At the divertor plate, the following Chodura's sheath condition is employed as

$$-\kappa_{\|}\nabla_{\|}T_e = C_e n_e v_{\|} T_e, \tag{13}$$

$$\nabla_{\|}T_i = 0, \tag{14}$$

$$v_{\|} = \sqrt{\frac{T_e + T_i}{\rho_i}}, \tag{15}$$

where C_e is equal to 1.8 when no secondary electron emission is considered.

[2]At the first wall,

He sets the free boundary condition.

[3] At the separatrix, parameter ranges are

$$0.2MW \le Q_t \le 0.8MW, \tag{16}$$

for the energy heat flux and

$$2\times10^{21}s^{-1} \le \Gamma \le 8\times10^{21}s^{-1}, \tag{17}$$

for the particle flux. The parameter survey has been done [12].

In the JFT-2M, the temperature profile at the inner plate becomes flat in the case that the toroidal field direction is counter clock wise. The simulation and experimental results are shown in Fig 8 and 9. He introduces

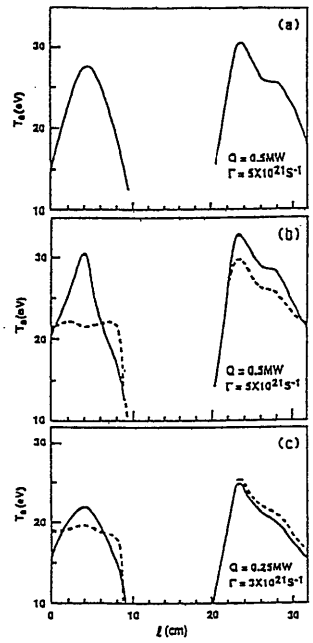

Fig. 8 Numerical result of the divertor temperature in JFT-2M. Solid line indicates the direction of the toroidal field is clock wise and dashed line for counter clock wise.(cited from Ref.[9]).

the drift heat flux ($\propto \mathrm{b}\times\nabla T_i$) into the ion heat flux q_{ψ}

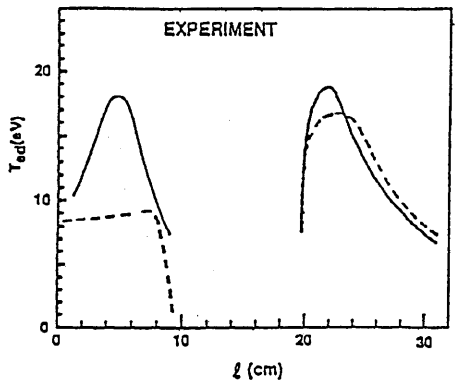

Fig. 9 Experimental result of the divertor temperature in JFT-2M. Solid line denotes the direction of the toroidal field is clock wise and dashed line for the case of counter clock wise. l is the length along the divertor plate as shown in the figure 7.(cited from Ref.[9]).

[10]. This simulation result agrees with the experimental result. This code is also used to analyze the effect of the limiter [13] and the L-to-H mode transition [14] on the SOL and divertor plasmas.

2.2.2 Anomalous transport models

If the transport of plasmas in magnetic confinement systems is due solely to Coulomb collisions then we would have a predictive theory (classical [15], or neoclassical [16] theory)available, however there is a strong evidence that transport is generally anomalously rapid - by up to two orders of magnitude in the case of electrons in Tokamaks, for instance. In this section we introduce anomalous transport models.

(1) Gyro-Bohm model [17, 18]

The vast majority of transport coefficients are based on turbulent transport due to fluctuations on a microscopic scale length such as Larmor radius, collisionless skin depth or resistive layer width. Using the Larmor radius, the generic gyro-Bohm transport coefficient is written as follows.

$$\chi_{e,i} = \frac{c_s \rho_s^2}{L_n} F_{e,i}(\nu_{*e}, \beta, \tau, m_e/m_i, q, s, \eta_i, \eta_e, \epsilon_n \ldots.), \tag{18}$$

where ν_{*e} is the electron collisionality, β is the ratio of thermal to magnetic energy, τ is the ratio of electron to ion temperature, m_j is the species mass, q is the safety factor, s is the magnetic shear, $\eta_i = |\nabla T_j| / |\nabla ln\, n_j|$ (where T_j and n_j are the species temperature and density), $L_n^{-1} = |\nabla ln\, n|$, $\epsilon_n = L_n/R$ and R is the major radius. We have also defined the sound speed, $c_s = \sqrt{T_e/m_i}$ and ion Larmor radius evaluated at the sound speed, $\rho_s = \sqrt{m_i T_e}/eB$. In practical units (ie, temperature in keV, magnetic field in Tesla, length scales in meters), the gyro-Bohm transport coefficient is written as

$$\chi_{e,i} = 3.23 \frac{\mu^{1/2} T_e^{3/2}}{B^2 L_n} F_{e,i}, \tag{19}$$

where μ is the ratio of the ion to proton mass.

(2) Rebut-Lallia-Watkins model [19, 20]

This inductive model combines an assumption that transport due to magnetic island formation switches on when a critical temperature gradient is exceeded, with empirical result from the power-balance studies to suggest a scaling for the electron thermal diffusivity (which is constructed in a dimensionally correct form). Chains of magnetic islands are assumed to exist, localized around rational surfaces although the detailed mechanism for their creation is not addressed in these first works. A chaotic region exists between the island chains when there is an overlapping of the islands and the existence of such a region leads to an enhanced transport. This is characterized by a stochasticity parameter, above which islands overlap and regions of stochastic magnetic field exist between them. It is argued that this happens when the electron temperature gradient exceeds a critical value. This critical value and anomalous diffusivity are obtained from inspection of Ohmic, L-mode and H-mode JET data.

Four dimensionless parameters are chosen to describe the dominant physical processes occurring in the tokamak, where plasma pressure represented by $\beta_p = 2\mu_0 p/B_\theta^2$, resistivity by $S = \eta J/(B_\theta u_{th})$, diamagnetic drift by $\Omega = (\nabla kT/eb_\theta v_t h)^2$ and power flow by $\Phi = P/(3\pi^2 rRnkTv_{th})$. JET data then suggests the following scalings for the critical temperature gradient and heat flux

$$\Omega_{ec} = S_e/\beta_{pe}, \quad \Phi_e = \Omega_i^{1/2} S_e^{1/2} \left(1 - (\Omega_{ec}/\Omega_e)^{1/2}\right), \tag{20}$$

where the subscripts i, e represent electron and ion quantities, respectively. One can also utilize certain dimensionless geometric factors such as aspect ratio, safety factor, etc. When these are taken into account, a critical temperature gradient of

$$(\nabla kT_e)_c = 0.06 \left[\frac{\eta J B^3}{n_e (kT)^{1/2}}\right]^{1/2} \left(\frac{1}{q}\right) \left(\frac{e^2}{\mu_0 m_e^{1/2}}\right)^{1/2} \tag{21}$$

is postulated (in SI units and with k being the Boltzmann constant). Note that η is the classical Spitzer resistivity and other parameters are standard. This implies

$$(\nabla kT_e) \propto \frac{\epsilon^{7/4} \nu_*^{1/2}}{\beta_e q^2} \frac{T_e}{a}. \tag{22}$$

The anomalous electron heat flux, F_e is taken to scale as

$$F_e = n_e \chi_e \nabla (kT_e) \left[1 - \left|\frac{\nabla T_e^c}{\nabla T_e}\right|\right] \tag{23}$$

with

$$\chi_e = 0.15\left[\frac{1}{L_{T_e}}+\frac{2}{L_{ne}}\right]\frac{\tau^{1/2}}{\epsilon}\left(\frac{q^2}{q'BR^{1/2}}\right)c^2(\mu_0 m_i)^{1/2}, \tag{24}$$

when the temperature gradient exceeds the critical value given in (21) and the radial derivative of the safety factor satisfies $q' > 0$ ($F_e = 0$ otherwise). Under the same conditions, the following expression for the anomalous ion heat transport is obtained:

$$F_i = n_i\chi_i\nabla(kT_i)\left[1-\left|\frac{\nabla T_e^c}{\nabla T_e}\right|\right] \tag{25}$$

with

$$\chi_i = \frac{\chi_e Z_i \tau^{1/2}}{\sqrt{1+Z_{eff}}} \tag{26}$$

where the Z_{eff} scaling is introduced in the later work by Taroni et al[21].

(3) Resistive ballooning mode model [22, 23]

In the limit of cylindrical geometry, where there is an unfavorable curvature, the mode is unstable and has interchange nature (and is thus termed the resistive interchange mode); it is relevant for a description of the transport in RFP's or stellarators where there is a bad curvature. In a tokamak the average curvature is good when $q > 1$ and therefore this mode is usually stable. However, tokamaks are truly toroidal, requiring a full toroidal treatment of the pressure-gradient driven mode. The mode then has a ballooning nature and the bad curvature region can dominate. This (resistive ballooning) mode may be unstable in a tokamak. The equation describing a plasma as a resistive fluid are invariant under certain sets of scaling transformations of the various plasma parameters. This invariance can be used to determine the dependence of the diffusivity on these parameters. In fact, if sufficient assumptions are made about the equations which govern the turbulence evolution then a complete scaling of the diffusivity can be derived. This has been done for the resistive pressure-gradient driven mode where two contributions to the transport are considered -a convective cross-field diffusion and a loss due to parallel transport along the stochastic magnetic field. The turbulence is considered in the following limits: $n \gg 1$, $n^2/S \ll 1$, $\beta q^2/\epsilon < 1$, where n is toroidal mode number, $S = \tau_R/\tau_A$ (with the resistive diffusion time, τ_R, and the poloidal Alfven time, τ_A, defined by $\tau_R = \mu_0 r^2/\eta$ and $\tau_A = (\mu_0\rho_m)^{1/2}Rq/B$, respectively, where η is the plasma resistivity and ρ_m is the mass density). Assuming that the diffusion coefficient scales as the square of a radial step size to a time step, the invariance transformations lead to the following result for the convective diffusion coefficient:

$$\chi = g_0\frac{\eta}{\mu_0}\left(\frac{\alpha}{s}\right) \tag{27}$$

where g_0 is a constant factor and

$$\alpha = -\frac{2\mu_0 Rq^2}{B^2}\frac{dp}{dr} \tag{28}$$

(4) Current diffusive ballooning mode model [24, 25, 26]

Itoh et al invoke a model involving anomalous electron viscosity in the Ohm's law. Introducing an anomalous field viscosity and thermal diffusivity in the vorticity and thermal equations respectively, they obtain an unstable ballooning mode. Assuming that the anomalous transport coefficients are all due to turbulence associated with this instability, they can be related through their quasilinear expressions. Their values when the corresponding turbulence is saturated can be obtained by demanding that the most unstable mode is marginally stable. The result for the fluid thermal diffusivity is

$$\chi = C_o\frac{V_A}{qR}\frac{c^2}{\omega_{pe}^2}\frac{\alpha^{3/2}}{s^{1/2}}, \tag{29}$$

where C_0 is a constant factor and

$$\alpha = -\frac{2\mu_0 Rq^2}{B^2}\frac{dp}{dr}. \tag{30}$$

3. Two Dimensional Transport Simulation in the SOL region

To understand the transport property in the SOL region, the analytical solution of two-dimensional transport equation is discussed for the various transport models [27].

In this chapter, we numerically solve two-dimensional transport equation in SOL region for various transport models and discuss the property of equilibrium temperature profile for each case. The time evolution of temperature is also discussed.

3.1 Analytical Solution of Temperature profile

The schematic configuration is shown in figure 10. The x-direction is taken along the magnetic field lines and y-direction is taken to be perpendicular to them.

Two-dimensional heat transport in the SOL region is governed by the equation

$$\frac{\partial T}{\partial t} = \frac{\partial}{\partial x}(\kappa_{\|}\frac{\partial T}{\partial x}) + \frac{\partial}{\partial y}(\kappa_{\perp}\frac{\partial T}{\partial y}), \tag{31}$$

where $\kappa_{\|}$ and $\kappa_{\perp}$ are the heat conductivities in the parallel and perpendicular directions to the magnetic field lines.

We employ the power law model for $\kappa_{\|}$ as

$$\kappa_{\|} = \kappa_{\|0}T^{\beta} \tag{32}$$

For the model of $\kappa_{\perp}$,

$$\kappa_{\perp} = \kappa_{\perp 0}T^{\alpha}|\nabla_{\perp}T|^{\gamma}, \tag{33}$$

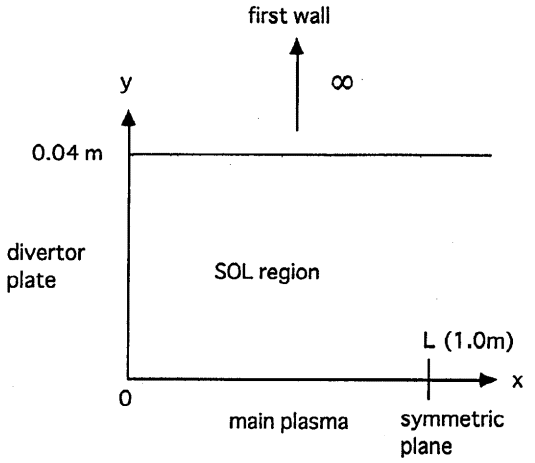

Fig. 10 Schematic configuration of a 2D scrape-off layer plasma. The line of $y = 0$ corresponds to the separatrix line. Along the x-axis, $x = 0$ corresponds to the divertor plate and $x = L$ is the symmetric plate. L is the connection length between the symmetric point and the divertor plate along the field line.

is assumed, where α, β, γ are constant valuables.

For the basic equation (31), we find the solution in the case which the separability of variables is satisfied. Namely,

$$T(x,y) = T_x(x)T_y(y) \tag{34}$$

We set the boundary condition as follows:

[1] at the separatrix (y=0)

$$P(x) = -\kappa_\perp \frac{\partial}{\partial y} T, \tag{35}$$

[2] at the inner wall

$$y \to \infty, \qquad T \to 0, \tag{36}$$

[3] at the symmetric plane (x=L)

$$\frac{\partial T}{\partial x} = 0, \tag{37}$$

where $P(x)$ is the power flux flows into the SOL region across the separatrix line.

At first, we shall transform the basic equation (31) into the equation which satisfies separability of variables. Substituting equations (32), (33) and (34) into (31), and setting $\frac{\partial}{\partial t} = 0$, we obtain

$$\kappa_{\|0} T_y^{\beta+1} \frac{d}{dx}\left\{T_x^\beta \frac{dT_x}{dx}\right\} = C(x,y) \tag{38}$$

and

$$\kappa_{\perp 0} T_x^{\alpha+\gamma+1} \frac{d}{dy}\left\{T_y^\alpha \left(\frac{dT_y}{dy}\right)^{\gamma+1}\right\} = -C(x,y). \tag{39}$$

Imposing separability of variables, the function $C(x,y)$ is to have the form

$$C(x,y) = -C_0 T_x^{\alpha+\gamma+1} T_y^{\beta+1}, \tag{40}$$

where C_0 is the eigenvalue. Substituting equation (40) in (38) and (39), we have

$$\frac{d}{dx}\left\{T_x^\beta \frac{dT_x}{dx}\right\} = -\frac{C_0}{\kappa_{\|0}} T_x^{\alpha+\gamma+1}, \tag{41}$$

$$\frac{d}{dy}\left\{T_y^\alpha \left(\frac{dT_y}{dy}\right)^{\gamma+1}\right\} = \frac{C_0}{\kappa_{\perp 0}} T_y^{\beta+1}. \tag{42}$$

Note that if we obtain a solution (T_x, T_y), the solution $(C_{xy}T_x, C_{xy}^{-1}T_y)$ (C_{xy} is an arbitrary numeric) satisfies (41)and (42). Here we consider the case $T_y(0) = 1$.

Next, we consider the boundary conditions. Substituting the equations (33),(34) into (35), we have

$$P(x) = -\kappa_{\perp 0} T_x^{\alpha+\gamma+1} \left(\frac{dT_y}{dy}\right)^{\gamma+1} T_y^\alpha \Big|_{y=0}. \tag{43}$$

Since $T_y = 1$ and $\frac{dT_y}{dy}$ is constant at y=0, $P(x)$ should be

$$P(x) = P_0 T_x^{\alpha+\gamma+1}, \tag{44}$$

where P_0 is the numeric coefficient.

So, at y=0, the numeric coefficient P_0 satisfies

$$\left(\frac{dT_y}{dy}\right)^{\gamma+1} = \frac{-P_0}{\kappa_{\perp 0}}. \tag{45}$$

And the condition (36) is rewritten as follows,

$$T_y \to 0, \ as \ y \to \infty. \tag{46}$$

Using these equations, we normalize the equations (41) and (42) as follows:

$$\frac{d^2}{d\hat{x}^2} X^{\beta+1} = -H X^{\alpha+\gamma+1} \tag{47}$$

and

$$\frac{d}{d\hat{y}}\left\{T_y^\alpha \left(\frac{dT_y}{d\hat{y}}\right)^{\gamma+1}\right\} = h T_y^{\beta+1}, \tag{48}$$

where $\hat{x} = \frac{x}{L}$, $\hat{y} = \frac{y}{\Delta_T}$ with

$$\Delta_T = \left(\frac{P_0}{\kappa_{\perp 0}}\right)^{\frac{1}{\gamma+1}}, \tag{49}$$

and the variable T_x is normalized by the value at the mid-plane $T_x(L)$, such as

$$X(x) = \frac{T_x(x)}{T_x(L)}. \tag{50}$$

The coefficient H and h is given by

$$H = (\beta+1)\frac{C_0 L^2}{\kappa_{\|0}} T_x(L)^{\alpha+\gamma-\beta} \tag{51}$$

and

$$h = \frac{C_0 \kappa_{\perp 0}^{\frac{1}{1+\gamma}}}{P_0^{\frac{2+\gamma}{1+\gamma}}}. \tag{52}$$

The parameter H denotes the profile of the heat flux from the core through the relation (44) and (51). When $H \simeq 0$, the heat flux from the core is (nearly) uniformly distributed along the separatrix. And if the value of H is large, the consistent heat flux distribution is more localized to the mid plane ($\hat{x} = 1$).

For this normalization, the boundary conditions is rewritten as

$$\frac{dT_y}{d\hat{y}} = -1 \ at \ \hat{y} = 0, \tag{53}$$

$$T_y \to 0, \ as \ \hat{y} \to 0, \tag{54}$$

$$X(\hat{x}) = 1, \ \frac{dX}{d\hat{x}} = 0, \ at \ \hat{x} = 0. \tag{55}$$

From the equations (48), (49), (53), and (54), the analytic solution T_y is obtained in the form

$$T_y(y) = \left\{ \frac{1}{1 + \left(\frac{\beta-\alpha-\gamma}{2+\gamma}\right) \triangle_T \, y} \right\}^{\frac{2+\gamma}{\beta-\alpha-\gamma}} \tag{56}$$

This analytical result shows that the difference between each transport models appears through the term proportional to $\triangle_T \, y$ in the denominator, where $\triangle_T$ represents the fall off length of the temperature in the y direction.

Multiplying the equation (47) by $\frac{d}{d\hat{x}} X^{\beta+1}$,

$$\frac{1}{2}\frac{d}{d\hat{x}}\left\{\frac{d}{d\hat{x}} X^{\beta+1}\right\}^2 = -\frac{H}{(\frac{\alpha+\gamma+1}{\beta+1}+1)}\frac{d}{d\hat{x}} X^{\alpha+\beta+\gamma+2} \tag{57}$$

is obtained.

Integrating equation (57) over $\hat{x}$ and imposing the boundary condition (55), we obtain the differential equation

$$\frac{d}{d\hat{x}} X^{\beta+1} = \sqrt{\frac{2(\beta+1)H}{\alpha+\beta+\gamma+2}} \sqrt{1 - X^{\alpha+\beta+\gamma+2}}. \tag{58}$$

Integrating this equation, we obtain the analytic solution of T(x,y) as

$$T(x,y) = X(x) T_x(L) T_y(y). \tag{59}$$

Now we examine the dependence of the analytic solution on the parameter $\triangle_T$ and H for the various transport models.

Parameter are chosen as

$$0 \ m \le x \le 1.0 \ m, \qquad 0 \ m \le y \le 0.04 \ m \tag{60}$$

and

$$T_x(L) = 80eV, \qquad T_y(0) = 1.0eV. \tag{61}$$

For the perpendicular heat conductivity, we consider the following models.

(1) Resistive ballooning mode model $(\alpha, \gamma) = (-\frac{3}{2}, 1)$

$$\kappa_\perp = \kappa_{\perp 0} T^{-\frac{3}{2}} \left|\frac{\partial T}{\partial y}\right|, \tag{62}$$

(2) Constant model $(\alpha, \gamma) = (0, 0)$

$$\kappa_\perp = \kappa_{\perp 0}, \tag{63}$$

(3) Bohm model $(\alpha, \gamma) = (1, 0)$

$$\kappa_\perp = \kappa_{\perp 0} T, \tag{64}$$

(4) Gyro-Bohm model $(\alpha, \gamma) = (\frac{3}{2}, 0)$

$$\kappa_\perp = \kappa_{\perp 0} T^{\frac{3}{2}}, \tag{65}$$

(5) ∇T model $(\alpha, \gamma) = (0, 1)$

$$\kappa_\perp = \kappa_{\perp 0} \left|\frac{\partial T}{\partial y}\right|, \tag{66}$$

(6) Rebut-like model $(\alpha, \gamma) = (-1, 1)$

$$\kappa_\perp = \kappa_{\perp 0} T^{-1} \left|\frac{\partial T}{\partial y}\right|, \tag{67}$$

(7) Current diffusive ballooning mode model $(\alpha, \gamma) = (0, \frac{3}{2})$

$$\kappa_\perp = \kappa_{\perp 0} \left|\frac{\partial T}{\partial y}\right|^{\frac{3}{2}}, \tag{68}$$

(8) Classical model $(\alpha, \gamma) = (-\frac{1}{2}, 0)$

$$\kappa_\perp = \kappa_{\perp 0} T^{-\frac{1}{2}}, \tag{69}$$

where $\kappa_{\|0}$ and $\kappa_{\perp 0}$ are constant.

For the parallel heat conductivity, we take the classical heat conductivity. That is,

$$\kappa_\| = \kappa_{\|0} T^{\frac{5}{2}}. \quad (\beta = \frac{5}{2}) \tag{70}$$

Using these models, we calculate the temperature profile in the SOL region.

At first, we consider the analytic solution $T_y(y)$.

From the equation (56), it is found that temperature decreases with increase of y.

The analytic solution T_y with $\triangle_T = 100$ is shown in the figure 11. It is found that the temperature near the first wall for the current diffusive ballooning mode model is lowest than other models, if $\triangle_T$ is common for all models.

Next we consider the analytic solution T_x. We examine the dependence on the parameter H.

It is found that the difference between each model in T_x is very small. The analytic solution T_x of the current diffusive ballooning mode model for various values of H is shown in the figure 12 as an example. It is seen that the temperature at the divertor plate decreases with the increase of the parameter H.

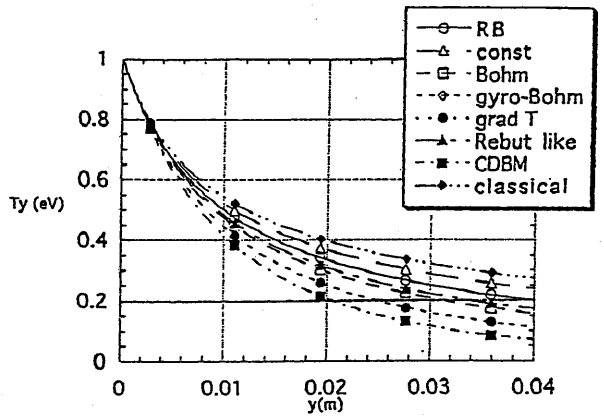

Fig. 11 The analytic solution T_y with $\Delta_T = 100$.

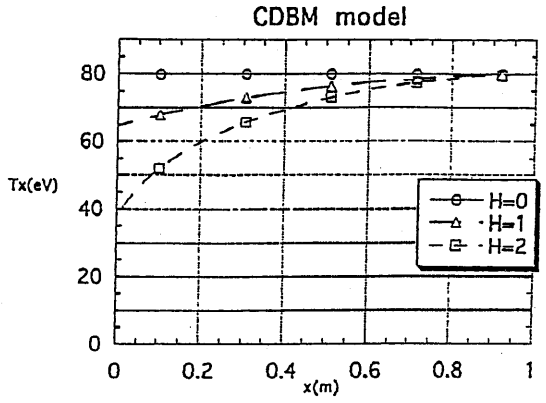

Fig. 12 The analytic solution T_x of the current diffusive ballooning mode model. The temperature at the divertor plate decrease with increase of the parameter H.

3.2 Two Dimensional Transport Model

In the previous chapter, we discuss the steady-state temperature profile in the SOL region for the various transport models. In this section, we investigate the time evolution of the temperature profile in the SOL region for the various transport models. For the parallel heat transport, we assume the classical heat conductivity. For the perpendicular heat transport, we take the classical heat conductivity and also the anomalous heat conductivities.

We solve the transport equation for the electron and examine the heat pulse propagation in the SOL region. The heat pulse is generated by the fluctuation at the edge of the bulk plasma, such as edge localized modes (ELMs). We analyze the deposition profile of heat pulse on the divertor plate.

Then, we consider the effect of the ion transport and also examine the heat pulse propagation.

3.2.1 The heat transport of the electrons in the SOL region

The basic equation for the electron is given by

$$\frac{\partial T_e}{\partial t} = \frac{\partial}{\partial x}(\chi_{\parallel} h^2 \frac{\partial T_e}{\partial x}) + \frac{\partial}{\partial y}(\chi_{\perp} \frac{\partial T_e}{\partial y}), \qquad (71)$$

where x-direction is taken along the main magnetic field lines and y-direction is taken to be perpendicular to the magnetic field lines and $h = B_\theta / B_t$ is the ratio of the strength of poloidal magnetic field and the toroidal magnetic field.

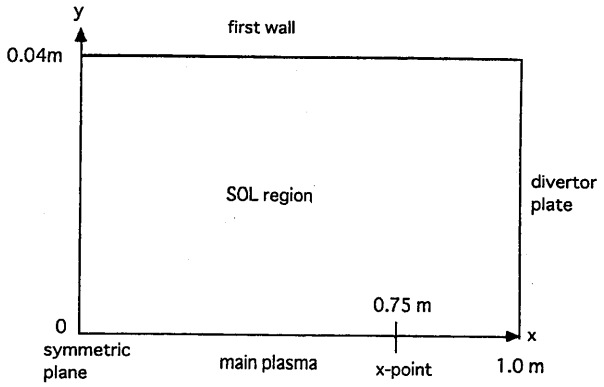

Fig. 13 Schematic configuration of a 2D SOL plasma.

The schematic configuration is presented in the figure 13. It should be noted that the co-ordinate system is different from that shown in figure 10, where the symmetric plane is taken at $x = L$. And boundary conditions [28] are given as

[1] at the symmetric plane

$$\frac{dT_e}{dx} = 0, \qquad (72)$$

[2] at the separatrix
from the symmetric plane to the x point (0.75m)

$$T_e = 80eV, \qquad (73)$$

from the x point to the divertor plate

$$\frac{dT_e}{dy} = 0, \qquad (74)$$

[3] at the wall

$$T_e = 2eV, \qquad (75)$$

[4] at the divertor plate

$$-\chi_{\parallel} \frac{dT_e}{dx} = \delta_e n_e T_e \sqrt{\frac{T_e}{m_i}}, \qquad (76)$$

where δ_e is the transmission coefficients [28, 29].

For the parallel heat conductivity, we take the classical heat conductivity,

$$\chi_{\parallel} = \frac{2}{3} \times 3.16 \frac{e}{m_e} \hat{\tau}_{ei} T_e^{\frac{5}{2}}. \tag{77}$$

For the perpendicular heat conductivity, we consider the classical heat conductivity and anomalous heat conductivities.

(1) the classical heat conductivity

$$\chi_{\perp} = \frac{2}{3} \times 4.66 \frac{m_e}{e} \frac{1}{B^2 \hat{\tau}_{ei}} T_e^{-\frac{1}{2}}, \tag{78}$$

with

$$\hat{\tau}_{ei} = \frac{25.8 \pi^{\frac{1}{2}} \epsilon_0^2 m_e^{\frac{1}{2}}}{n_e Z_{eff} e^{\frac{5}{2}} ln\Lambda}. \tag{79}$$

(2) the resistive ballooning mode model

$$\chi_{\perp} = \frac{2}{3} C_{RB} \frac{m_e}{e} \frac{Rq^2}{sB^2 \hat{\tau}_{ei}} T_e^{-\frac{3}{2}} \left(-\frac{dT_e}{dy} \right) \tag{80}$$

(3) the constant model

$$\chi_{\perp} = \frac{2}{3} C_{const} \tag{81}$$

(4) the Bohm model

$$\chi_{\perp} = \frac{2}{3} C_{Bohm} \frac{T_e}{eB} \tag{82}$$

(5) the current diffusive ballooning mode model

$$\chi_{\perp} = \frac{2}{3} C_{CDBM} \frac{\nu_A}{qR} \frac{c^2}{\omega_{pe}^2} \frac{1}{s^{\frac{1}{2}}} \left(\frac{2\mu_0 Rq^2}{B^2} \right)^{\frac{3}{2}} \left(-\frac{dT_e}{dy} \right)^{\frac{3}{2}} \tag{83}$$

We set parameters in these heat conductivity models as follows.

$n_e = 1.0 \times 10^{19} m^{-3}$, $h = \frac{B_p}{B} = 0.06$, $\delta_e = 0.005$, $Z_{eff} = 1.$, $R = 1.2m$,

$q = 3$, $s = \frac{4}{3}$, $B = 1T$, $C_{RB} = C_{const} = C_{CDBM} = 10.$, $C_{Bohm} = 1.0$,

$ln\Lambda = 20$.

Since the heat conductivity of the Bohm model is larger than that of the other models, we set the numerical constant value C of these models 10 so that the magnitudes of these models are comparable.

Figure 14 shows the two-dimensional steady state temperature profile for the Bohm model. Near the divertor plate ($x \approx 1m$), the temperature profile along the field line does not change so much from that of x-point (0.75m). For the other models, the similar tendency is observed. The reason is considered to be due to the boundary condition at divertor plate. In our code, we take the finite difference algorithm for the boundary condition (76) such as

$$T_e(nx+1, j) = \left(T_e(nx-1, j)^{5/2} - 5.0 \times A \times dx \times \delta_e \right)^{2/5}, \tag{84}$$

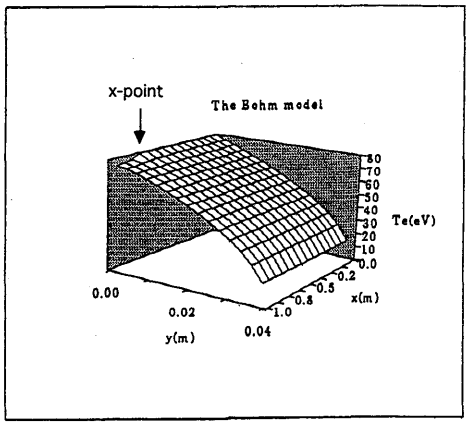

Fig. 14 The 2D electron temperature profile for the Bohm model.

with

$$A = \frac{\sqrt{\frac{e}{m_i}}}{\left[1.5 \times h \times \left(\frac{2}{3} \times 3.16 \frac{e}{m_e} \hat{\tau}_{ei} \right) \right]}, \tag{85}$$

$$nx = 30, \quad dx = \frac{1}{nx} = 0.03333, \tag{86}$$

where dx is the size of the mesh of x direction, j is the mesh number to the y direction and nx is the mesh number at the divertor plate. For the large value of δ_e, $T_e(nx+1, j)$ becomes imaginary. To ensure the condition that T_e is real, we should set $\delta_e < 0.005$ so that almost $\frac{dT_e}{dx} \simeq 0$ (zero parallel heat flux condition) is imposed at the divertor plate.

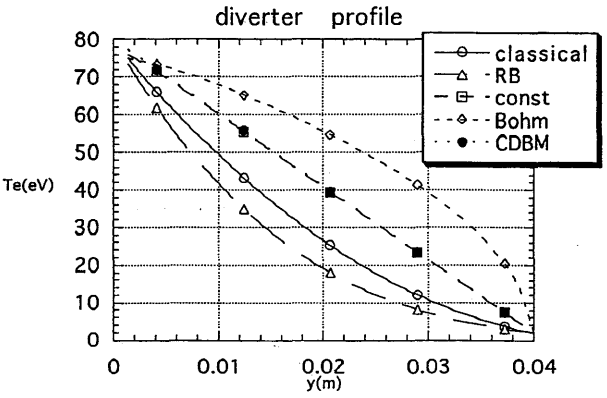

Fig. 15 The electron temperature profile at the divertor plate.

The temperature profile at the divertor plate is shown in figure 15. The temperature of the Bohm model is found to be higher than that of the other models in the whole region of divertor plate.

If we consider a minimum temperature of the divertor plate to be 30 eV, for example, it suggests that we should cool the divertor plate for the whole region if the transport process is governed by the Bohm type. If the transport governed by the classical model or resistive

ballooning mode model, we only need to cool the plate near the separatrix.

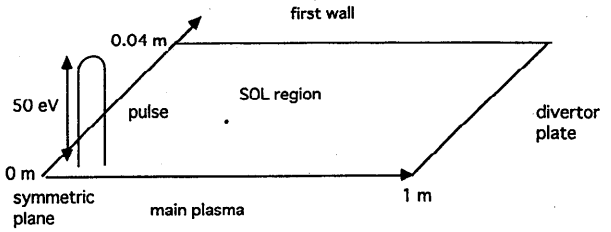

Fig. 16 The temperature fluctuation near the symmetric plane with the amplitude 50eV.

Next, we examine the heat pulse propagation in the SOL region. In the steady state of SOL plasma, we add the temperature perturbation near the symmetric plane with it's amplitude 50 eV as is shown in the figure 16, so that the heat pulse is introduced in the SOL region. This heat pulse propagates in the SOL region and is transmitted to the divertor plate according to these transport models.

The increment of the temperature at the divertor plate is examined. The result is shown in the figure 17. Among the models, the time at which the heat pulse

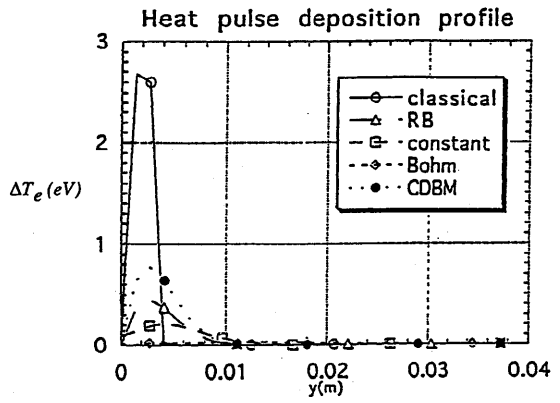

Fig. 17 The electron heat pulse deposition profile at the divertor plate.

reaches at the divertor plate isn't so much different and heat pulse arrives at near the separatrix on the plate. The typical time scale is governed by the parallel thermal conductivity and is order of 5.0×10^{-7} s for these parameters. The amount of heat pulse of the classical transport model which reaches at the plate is larger than those of other models. Similar to the result in figure 15, the width of heat pulse profile of classical model is narrower than those of other models. In our code, if the amplitude of the heat pulse is exceed 50 eV, the numerical instability occurs. To speculate the effect of the large heat pulse, we examine the dependence of the peak value of the temperature increment at the divertor plate on the amplitude of the heat pulse. The result is shown in figure 18. There is a linear relation between the temperature increment and the amplitude of the heat pulse for all models. From the figures 17 and 18, for the large heat pulse, we conjecture that for the classical model, the temperature increment at the divertor plate is larger than those of other models and it occurs near the separatrix, For other models, the temperature increment would be small, however the heat pulse profile spans in the wide region of divertor plate.

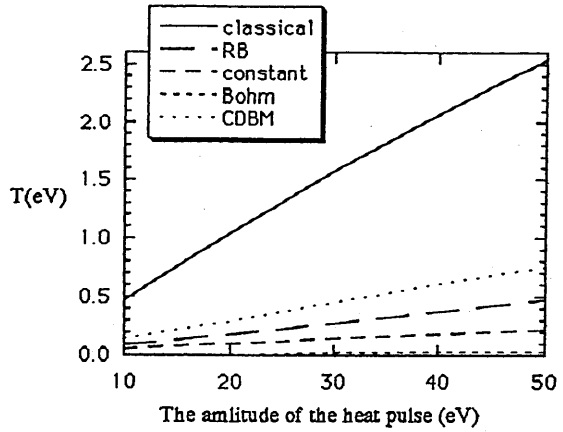

Fig. 18 The dependence of the peak value of the electron temperature increment at the divertor plate on the amplitude of the heat pulse.

3.2.2 The heat transport of the electrons and ions in the SOL region

In the previous section, we investigate the transport of the electrons. In this section, we consider the ion transport in the SOL region, and analyze the heat pulse propagation.

The ion heat transport equation and boundary conditions are given as follows. The basic equation is the same as those for the electron except the parallel heat conductivity

$$\chi_{\parallel} = \frac{2}{3} \times 3.9 \frac{e}{m_i} \hat{\tau}_{ii} T_i^{\frac{5}{2}}, \tag{87}$$

where

$$\hat{\tau}_{ii} = \frac{25.8\pi^{\frac{1}{2}} \epsilon_0^2 m_i^{\frac{1}{2}}}{n_i Z_{eff} e^{\frac{5}{2}} ln\Lambda}. \tag{88}$$

We assume the quasi-neutrality condition

$$n_i = n_e. \tag{89}$$

For the perpendicular heat conductivity, we assume the anomalous heat conductivities, which are the same

as those for electrons. The classical heat conductivity given by

$$\chi_\perp = \frac{2}{3} \times 2\frac{m_i}{e}\frac{1}{B^2\hat{\tau}_{ii}}T_i^{-\frac{1}{2}}. \quad (90)$$

The boundary condition is taken in the same way as for electrons except at the divertor plate.

At the divertor plate the conditions are taken for the electrons

$$-\chi_{\|e}\frac{dT_e}{dx} = \delta_e n_e T_e\sqrt{\frac{T_e+T_i}{m_i}}, \quad (91)$$

and for the ions

$$-\chi_{\|i}\frac{dT_i}{dx} = \delta_i n_i T_i\sqrt{\frac{T_e+T_i}{m_i}}. \quad (92)$$

We use the same parameters as those used in the previous section.

When we set $\delta_e = \delta_i = 0.005$, the boundary conditions (91) and (92) are almost equivalent to the condition $\frac{dT_e}{dx} \simeq 0$ and $\frac{dT_i}{dx} \simeq 0$. The ion temperature profile at the divertor plate is shown in the figure 19. The 2D

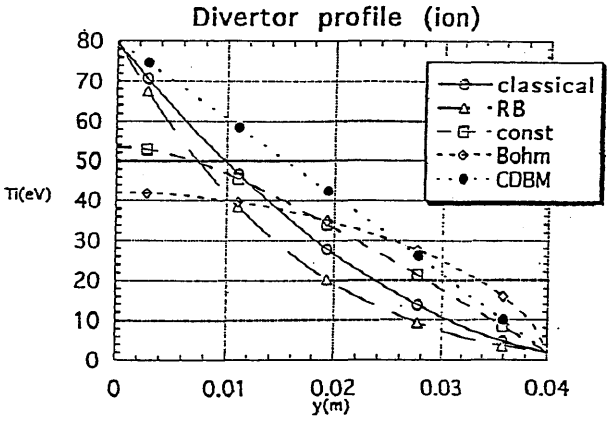

Fig. 19 The ion temperature profile at the divertor plate.

temperature profile for the Bohm model is shown in the figure 20.

The difference between the electron and ion temperature profiles is clearly observed for the Bohm model and the constant model. This is because for all models, the parallel ion heat conductivity is smaller than the electron's so that the perpendicular ion heat conductivity is effective compared with the perpendicular electron heat conductivity, namely, $\frac{\chi_{\perp i}}{\chi_{\|i}} > \frac{\chi_{\perp e}}{\chi_{\|e}}$.

Figure 21 shows the profile of the perpendicular ion heat conductivity at the divertor plate. The Bohm model and the constant model have large heat conductivity near the separatrix, which leads to the drop of ion temperature in this region. On the other hand, the drop of electron temperature is not so strong in other models due to the large parallel heat conductivity.

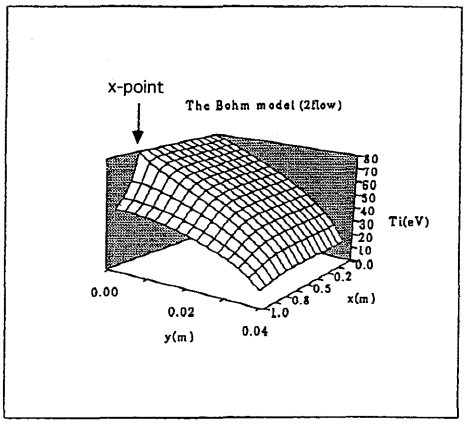

Fig. 20 The 2D ion temperature profile for the Bohm model.

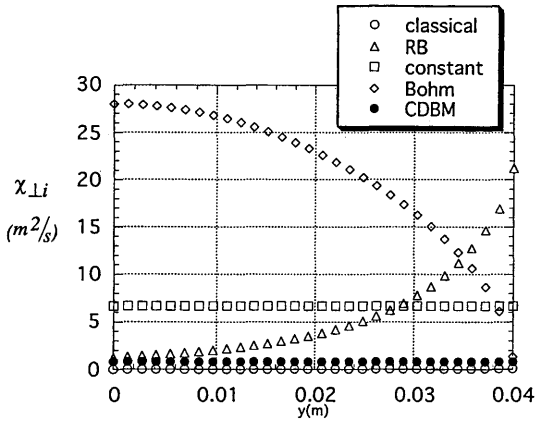

Fig. 21 The profile of the perpendicular ion heat conductivity at the divertor plate.

Next we analyze the heat pulse propagation in the SOL region. The electron heat pulse propagation is analyzed in the previous section. In the same way, we analyze the ion heat pulse propagation. The result is shown in the figure 22. Because the ion parallel heat conduc-

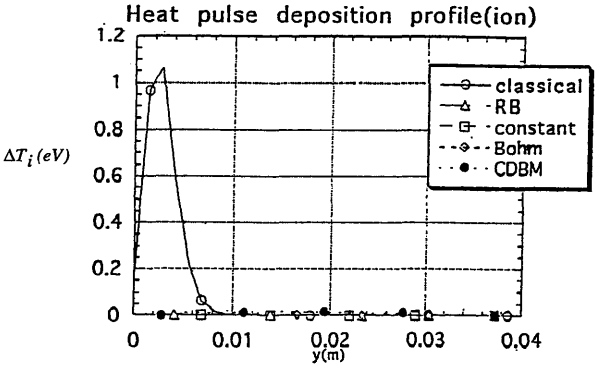

Fig. 22 The ion heat pulse deposition profile at the divertor plate.

tivity is about 40 times smaller than that of the elec-

trons, the perpendicular diffusion smears out the heat pulse. The arrival of the ion heat pulse at the divertor plate is not clearly observed, except for the classical model although it's amplitude is smaller than that of the electrons. We also examine the dependence of the peak value of the temperature increment at the divertor plate on the amplitude of the heat pulse. The result is shown in the figure 23. For the classical model, the same

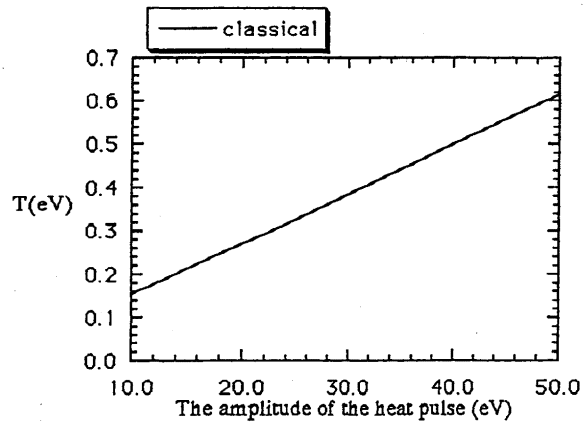

Fig. 23 The dependence of the peak value of the ion temperature increment at the divertor plate on the amplitude of the heat pulse.

linear relation between the temperature increment and the amplitude of the heat pulse is obserbed as in the case of the electron. However for the anomalous transport models, the increment of the temperature at the divertor plate is found very small.

3.3 Summary of simulation result

In this chapter, we show the analytic solutions for the various heat conductivity models. From these analytic solutions, we find the common feature of transport models as follows.

The analytic solution T_y decreases with the increment of the value $\triangle_T$. The parameter H denotes the profile of the heat flux from the core. When $H \simeq 0$, the heat flux from the core is uniformly distributed along the separatrix. And if the value of H is large, the consistent heat flux distribution is more localized to the mid plane. The temperature at the divertor plate decreases with increment of the value H.

Next, we solve the time dependent transport equation for the electron. We find that the transport governed by the Bohm model burdens the divertor plate compared with those of other models. The temperature at the divertor plate is expected to be higher than those of other models in the whole region. If, it is the case, the cooling of the divertor plate for the whole region is necessary. If the classical heat transport model or the resistive ballooning mode model applies, we only need to cool the plate near the separatrix.

We also analyze the heat pulse propagation in the SOL region. If the transport is governed by the classical transport process, the large amount of the heat pulse reaches at the divertor plate. For the classical model, the effect of the heat pulse is localized near the separatrix. On the other hand, the width of heat pulse for the other models is larger than that of classical model, however it's amplitude is small. There is a linear relation between the increment of the temperature and the amplitude of the heat pulse.

We solve the ion transport equation as well. The difference between the electron and the ion temperature profiles is clearly observed for the Bohm model and the constant model. With respect to the Bohm model and constant model, the ion temperature rapidly decreases from the x-point to the divertor plate. This is because the relation $\frac{\chi_{\perp i}}{\chi_{\parallel i}} > \frac{\chi_{\perp e}}{\chi_{\parallel e}}$ is hold and the perpendicular heat conductivity of these models near the separatrix is larger than those of other models.

Furthermore we examine the ion heat pulse propagation in the SOL region. The amount of the heat pulse carried by the ions to the divertor plate is smaller than that by the electrons for all models. This is because the perpendicular diffusion smears out the heat pulse. On the other hand, for the classical transport model, the large amount of the ion heat pulse is transported to the divertor plate compared with those of other models.

4. Summary and Discussions

In Chapter 2, we review the experiments. ELM events are needed to keep the good confinement mode, called the H-mode. However, a large amount of particle and heat flux bursts out from the main plasma. These particle and heat fluxes are transported to the divertor plate and promote the impurity production. To avoid this situation, the detached divertor experiment which controls the ion flow in the SOL region is examined. It is also necessary to understand the detailed physics of divertor plasma as well as its operation boundary. For this purpose, we introduce the various transport models and examine the transport process in the SOL region, some of which are explained in the Chapter 2. In the Chapter 3, we give the analytic solution for the various transport models for which the separability of the variables in the SOL region is assumed. This analytic solution depends on the parameter $\triangle_T$ and H. $\triangle_T$ represents the fall off length of the temperature in the y direction (across the magnetic field line) and H denotes the profile of the heat flux from the core. The analytic solution T_y decreases with the increment of the parameter $\triangle_T$. The temperature at the divertor plate decreases with the increment of the value H, and the heat flux distribution is more localized to the midplane. Next we examine the time

evolution of the electron temperature for various transport models in the SOL region. Steady state solutions of temperature profiles are obtained. We find that the transport governed by the Bohm model is more serious for the heat load of the divertor plate than those of the other models. The temperature at the divertor plate is expected to be higher in the whole region so that the cooling the divertor plate for whole region is necessary. If the classical heat transport process or the resistive ballooning mode model process applies, we find that the stronger cooling the divertor plate near the separatrix may be necessary. We analyze the electron heat pulse propagation in the SOL region in order to simulate the propagation of ELM burst. If the transport is governed by the classical transport process, the large and localized heat pulse reaches at the divertor plate. If the anomalous transport prevails, the broaden pulse may reach to the plate. There is a linear relation between the increment of the temperature and the amplitude of the heat pulse. The increment of the temperature at the divertor plate in the classical model is larger than those of the other models and it is localized at the separatrix. On the other hand, the increment of the temperature for other models occurs in the wider region, although the amplitude is smaller than that of the classical model. We also solve the ion transport equation. The difference between the electron and the ion temperature profiles is clearly observed for the Bohm model and the constant model. In this case, the ion temperature decreases from the x-point to the divertor plate drastically. This is because the relation $\frac{\chi_{\perp i}}{\chi_{\parallel i}} > \frac{\chi_{\perp e}}{\chi_{\parallel e}}$ is hold, therefore the perpendicular ion conductivity is effective compared with the perpendicular electron conductivity. Furthermore, the perpendicular ion heat conductivities of these models near the separatrix are larger than those of other models.

We analyze the ion heat pulse propagation. The arrival of the ion heat pulse at the divertor plate is not clearly observed, except for the classical model. This is because the perpendicular diffusion smears out the heat pulse. For the classical model, the linear relation between the temperature increment and the amplitude of the heat pulse is obtained as in the case of the electron heat pulse propagation. However, for the anomalous transport models, the increment of the temperature at the divertor plate is very small for the parameter ranges of our analysis.

In this paper, 2D transport model equations are solved and the heat pulse propagations in the SOL region are analyzed. However, we do not take into account of the flow effects. Such effects may be important for the heat pulse propagation. As for a future work, the more complete set of equations described in Capter 2 should be solved and heat pulse propagations are to be investigated for the various transport models in the SOL region. To take account of the geometrical effect of the scrape-off layer is also important.

References

1) Wagner F and the ASDEX team 1982 *Phys. Rev. Lett* **49** 1408
2) Wagner F, et al 1982 *Plasma Physics and Controlled Nuclear Fusion Research (Proc. 9th Int.Conf. (Baltimore 1982))* Vol 1 (Vienna: IAEA) 43
3) Burell K H, et al 1983 *Controlled Fusion and Plasma Physics (Proc. 11th Europe.Conf. (Aachen 1983))* Part I 11
4) Kaye S M, et al 1983 *Controlled Fusion and Plasma Physics (Proc. 11th Europe.Conf. (Aachen 1983))* Part I 19
5) Keilhacker M 1984 *Plasma Physics and Controlled Nuclear Fusion Research* Vol 1 (Vienna: IAEA) 71
6) Zohm H 1996 *Plasma Phys. Control. Fusion* **38** 105
7) Wagner F, Keilhacker M, et al 1984 *Journal of Nuclear Materials* **121** 103
8) Loarte A, et al 1997 *JET Report* JET-P(97)03
9) Ueda N 1996 *Jornal of Plasma and Fusion Research* **72** No 9 874
10) Ueda N, Itoh K, Itoh S-I et al 1989 *Journal of Nuclear Materials* **162-164** 607
11) Ueda N, Kasai M, Tanaka M, Sugihara M and Sengoku S 1988 *Nucl. Fusion* **28** 1183
12) Itoh S-I, Ueda N and Itoh K 1990 *Plasma Phys. Control. Fusion* **32** 415
13) Ueda N, Itoh K and Itoh S-I 1989 *Nucl. Fusion* **29** 173
14) Itoh S-I, Itoh K, Ohkawa T and Ueda N, Itoh K and Itoh S-I *Plasma Physics and Controlled Nuclear Fusion Research (Proc. 12th Int.Conf. (Washington 1988))* Vol 2 (Vienna: IAEA) 23
15) Braginskii S I 1966 *Rev. of Plasma Physics* Vol.4 205
16) Kadomtsev B B and Pogutse O P 1971 *Nucl. Fusion* **11** 67
17) Connor J W 1988 *Plasma Phys. Control. Fusion* **30** 619
18) Hugon M and Rebut P H 1991 *Plasma Physics and Controlled Nuclear Fusion Research (Proc. 13th Int.Conf. (Washington 1990))* Vol 2 (Vienna: IAEA) 45

19) Lallia P P, Rebut P H and Watkins M L 1988 *JET Report* JET-P(88)05

20) Rebut P H, Lallia P P and Watkins M L 1989 *Plasma Physics and Controlled Nuclear Fusion Research (Proc. 12th Int. Conf. (Nice, 1988))* Vol 2 (Vienna: IAEA) 191

21) Taroni A et al 1991 *Plasma Physics and Controlled Nuclear Fusion Research (Proc. 13th Int. Conf. (Washinton, 1990))* Vol 1 (Vienna: IAEA) 93

22) Connor J W and Taylor J B 1984 *Phys. Fluids* **27** 2679

23) Carreras B A, et al 1983 *Phys. Rev. Lett* **50** 503

24) Itoh K, Itoh S-I, Fukuyama A, Yagi M and Azumi M 1994 *Plasma Phys. Control. Fusion* **36** 279

25) Itoh K, Itoh S-I, Fukuyama A, 1999 *Transport and Structural Formation in Plasmas* 155

26) Connor J W 1993 *Plasma Phys. Control. Fusion* **35** 757

27) Itoh S-I, Yagi M and Itoh K 1995 *Plasma Phys. Control. Fusion* **37** 155

28) Braams B J, et al 1984 *Journal of Nuclear Materials* **121** 75

29) Vold E L, Najimabadi F, and Conn R W 1991 *Phys. Fluids B 3* **11** 3132